

The multiplicity dependence of inclusive p_t spectra from p-p collisions at $\sqrt{s} = 200$ GeV

J. Adams,² M.M. Aggarwal,²⁹ Z. Ahammed,⁴⁴ J. Amonett,¹⁹ B.D. Anderson,¹⁹ M. Anderson,⁶ D. Arkhipkin,¹² G.S. Averichev,¹¹ Y. Bai,²⁷ J. Balewski,¹⁶ O. Barannikova,² L.S. Barnby,² J. Baudot,¹⁷ S. Bekele,²⁸ V.V. Belaga,¹¹ A. Bellingeri-Laurikainen,³⁹ R. Bellwied,⁴⁷ F. Benedosso,²⁷ B.I. Bezverkhny,⁴⁹ S. Bhardwaj,³⁴ A. Bhasin,¹⁸ A.K. Bhati,²⁹ H. Bichsel,⁴⁶ J. Bielcik,⁴⁹ J. Bielcikova,⁴⁹ L.C. Bland,³ C.O. Blyth,² S-L. Blyth,²¹ B.E. Bonner,³⁵ M. Botje,²⁷ J. Bouchet,³⁹ A.V. Brandin,²⁵ A. Bravar,³ M. Bystersky,¹⁰ R.V. Cadman,¹ X.Z. Cai,³⁸ H. Caines,⁴⁹ M. Calderón de la Barca Sánchez,⁶ J. Castillo,²⁷ O. Catu,⁴⁹ D. Cebra,⁶ Z. Chajecski,²⁸ P. Chaloupka,¹⁰ S. Chattopadhyay,⁴⁴ H.F. Chen,³⁷ J.H. Chen,³⁸ Y. Chen,⁷ J. Cheng,⁴² M. Cherney,⁹ A. Chikhanian,⁴⁹ H.A. Choi,³³ W. Christie,³ J.P. Coffin,¹⁷ T.M. Cormier,⁴⁷ M.R. Cosentino,³⁶ J.G. Cramer,⁴⁶ H.J. Crawford,⁵ D. Das,⁴⁴ S. Das,⁴⁴ M. Daugherty,⁴¹ M.M. de Moura,³⁶ T.G. Dedovich,¹¹ M. DePhillips,³ A.A. Derevschikov,³¹ L. Didenko,³ T. Dietel,¹³ P. Djawotho,¹⁶ S.M. Dogra,¹⁸ W.J. Dong,⁷ X. Dong,³⁷ J.E. Draper,⁶ F. Du,⁴⁹ V.B. Dunin,¹¹ J.C. Dunlop,³ M.R. Dutta Mazumdar,⁴⁴ V. Eckardt,²³ W.R. Edwards,²¹ L.G. Efimov,¹¹ V. Emelianov,²⁵ J. Engelage,⁵ G. Eppley,³⁵ B. Erazmus,³⁹ M. Estienne,¹⁷ P. Fachini,³ R. Fatemi,²² J. Fedorisin,¹¹ K. Filimonov,²¹ P. Filip,¹² E. Finch,⁴⁹ V. Fine,³ Y. Fisyak,³ J. Fu,⁴⁸ C.A. Gagliardi,⁴⁰ L. Gaillard,² J. Gans,⁴⁹ M.S. Ganti,⁴⁴ V. Ghazikhanian,⁷ P. Ghosh,⁴⁴ J.E. Gonzalez,⁷ Y.G. Gorbunov,⁹ H. Gos,⁴⁵ O. Grebenyuk,²⁷ D. Grosnick,⁴³ S.M. Guertin,⁷ K.S.F.F. Guimaraes,³⁶ Y. Guo,⁴⁷ N. Gupta,¹⁸ T.D. Gutierrez,⁶ B. Haag,⁶ T.J. Hallman,³ A. Hamed,⁴⁷ J.W. Harris,⁴⁹ W. He,¹⁶ M. Heinz,⁴⁹ T.W. Henry,⁴⁰ S. Hepplemann,³⁰ B. Hippolyte,¹⁷ A. Hirsch,³² E. Hjort,²¹ G.W. Hoffmann,⁴¹ M.J. Horner,²¹ H.Z. Huang,⁷ S.L. Huang,³⁷ E.W. Hughes,⁴ T.J. Humanic,²⁸ G. Igo,⁷ P. Jacobs,²¹ W.W. Jacobs,¹⁶ P. Jakl,¹⁰ F. Jia,²⁰ H. Jiang,⁷ P.G. Jones,² E.G. Judd,⁵ S. Kabana,³⁹ K. Kang,⁴² J. Kapitan,¹⁰ M. Kaplan,⁸ D. Keane,¹⁹ A. Kechechyan,¹¹ V. Yu. Khodyrev,³¹ B.C. Kim,³³ J. Kiryluk,²² A. Kisiel,⁴⁵ E.M. Kislov,¹¹ S.R. Klein,²¹ D.D. Koetke,⁴³ T. Kollegger,¹³ M. Kopytine,¹⁹ L. Kotchenda,²⁵ V. Kouchpil,¹⁰ K.L. Kowalik,²¹ M. Kramer,²⁶ P. Kravtsov,²⁵ V.I. Kravtsov,³¹ K. Krueger,¹ C. Kuhn,¹⁷ A.I. Kulikov,¹¹ A. Kumar,²⁹ A.A. Kuznetsov,¹¹ M.A.C. Lamont,⁴⁹ J.M. Landgraf,³ S. Lange,¹³ S. LaPointe,⁴⁷ F. Laue,³ J. Lauret,³ A. Lebedev,³ R. Lednicky,¹² C-H. Lee,³³ S. Lehocka,¹¹ M.J. LeVine,³ C. Li,³⁷ Q. Li,⁴⁷ Y. Li,⁴² G. Lin,⁴⁹ S.J. Lindenbaum,²⁶ M.A. Lisa,²⁸ F. Liu,⁴⁸ H. Liu,³⁷ J. Liu,³⁵ L. Liu,⁴⁸ Z. Liu,⁴⁸ T. Ljubicic,³ W.J. Llope,³⁵ H. Long,⁷ R.S. Longacre,³ M. Lopez-Noriega,²⁸ W.A. Love,³ Y. Lu,⁴⁸ T. Ludlam,³ D. Lynn,³ G.L. Ma,³⁸ J.G. Ma,⁷ Y.G. Ma,³⁸ D. Magestro,²⁸ D.P. Mahapatra,¹⁴ R. Majka,⁴⁹ L.K. Mangotra,¹⁸ R. Manweiler,⁴³ S. Margetis,¹⁹ C. Markert,¹⁹ L. Martin,³⁹ H.S. Matis,²¹ Yu.A. Matulenko,³¹ C.J. McClain,¹ T.S. McShane,⁹ Yu. Melnick,³¹ A. Meschanin,³¹ M.L. Miller,²² N.G. Minaev,³¹ S. Mioduszewski,⁴⁰ C. Mironov,¹⁹ A. Mischke,²⁷ D.K. Mishra,¹⁴ J. Mitchell,³⁵ B. Mohanty,⁴⁴ L. Molnar,³² C.F. Moore,⁴¹ D.A. Morozov,³¹ M.G. Munhoz,³⁶ B.K. Nandi,¹⁵ C. Nattrass,⁴⁹ T.K. Nayak,⁴⁴ J.M. Nelson,² P.K. Netrakanti,⁴⁴ V.A. Nikitin,¹² L.V. Nogach,³¹ S.B. Nurushev,³¹ G. Odyniec,²¹ A. Ogawa,³ V. Okorokov,²⁵ M. Oldenburg,²¹ D. Olson,²¹ M. Pachr,¹⁰ S.K. Pal,⁴⁴ Y. Panebratsev,¹¹ S.Y. Panitkin,³ A.I. Pavlinov,⁴⁷ T. Pawlak,⁴⁵ T. Peitzmann,²⁷ V. Perevoztchikov,³ C. Perkins,⁵ W. Peryt,⁴⁵ V.A. Petrov,⁴⁷ S.C. Phatak,¹⁴ R. Picha,⁶ M. Planinic,⁵⁰ J. Pluta,⁴⁵ N. Poljak,⁵⁰ N. Porile,³² J. Porter,⁴⁶ A.M. Poskanzer,²¹ M. Potekhin,³ E. Potrebenikova,¹¹ B.V.K.S. Potukuchi,¹⁸ D. Prindle,⁴⁶ C. Pruneau,⁴⁷ J. Putschke,²¹ G. Rakness,³⁰ R. Raniwala,³⁴ S. Raniwala,³⁴ R.L. Ray,⁴¹ S.V. Razin,¹¹ J. Reinnarth,³⁹ D. Relyea,⁴ F. Retiere,²¹ A. Ridiger,²⁵ H.G. Ritter,²¹ J.B. Roberts,³⁵ O.V. Rogachevskiy,¹¹ J.L. Romero,⁶ A. Rose,²¹ C. Roy,³⁹ L. Ruan,²¹ M.J. Russcher,²⁷ R. Sahoo,¹⁴ I. Sakrejda,²¹ S. Salur,⁴⁹ J. Sandweiss,⁴⁹ M. Sarsour,⁴⁰ P.S. Sazhin,¹¹ J. Schambach,⁴¹ R.P. Scharenberg,³² N. Schmitz,²³ K. Schweda,²¹ J. Seger,⁹ I. Selyuzhenkov,⁴⁷ P. Seyboth,²³ A. Shabetai,²¹ E. Shahaliev,¹¹ M. Shao,³⁷ M. Sharma,²⁹ W.Q. Shen,³⁸ S.S. Shimanskiy,¹¹ E. Sichtermann,²¹ F. Simon,²² R.N. Singaraju,⁴⁴ N. Smirnov,⁴⁹ R. Snellings,²⁷ G. Sood,⁴³ P. Sorensen,³ J. Sowinski,¹⁶ J. Speltz,¹⁷ H.M. Spinka,¹ B. Srivastava,³² A. Stadnik,¹¹ T.D.S. Stanislaus,⁴³ R. Stock,¹³ A. Stolpovsky,⁴⁷ M. Strikhanov,²⁵ B. Stringfellow,³² A.A.P. Suaide,³⁶ E. Sugarbaker,²⁸ M. Sumera,¹⁰ Z. Sun,²⁰ B. Surrow,²² M. Swanger,⁹ T.J.M. Symons,²¹ A. Szanto de Toledo,³⁶ A. Tai,⁷ J. Takahashi,³⁶ A.H. Tang,³ T. Tarnowsky,³² D. Thein,⁷ J.H. Thomas,²¹ A.R. Timmins,² S. Timoshenko,²⁵ M. Tokarev,¹¹ T.A. Trainor,⁴⁶ S. Trentalange,⁷ R.E. Tribble,⁴⁰ O.D. Tsai,⁷ J. Ulery,³² T. Ullrich,³ D.G. Underwood,¹ G. Van Buren,³ N. van der Kolk,²⁷ M. van Leeuwen,²¹ A.M. Vander Molen,²⁴ R. Varma,¹⁵ I.M. Vasilevski,¹² A.N. Vasiliev,³¹ R. Vernet,¹⁷ S.E. Vigdor,¹⁶ Y.P. Viyogi,⁴⁴ S. Vokal,¹¹ S.A. Voloshin,⁴⁷ W.T. Waggoner,⁹ F. Wang,³² G. Wang,⁷ J.S. Wang,²⁰ X.L. Wang,³⁷ Y. Wang,⁴² J.W. Watson,¹⁹ J.C. Webb,⁴³ G.D. Westfall,²⁴ A. Wetzler,²¹ C. Whitten Jr.,⁷ H. Wieman,²¹ S.W. Wissink,¹⁶ R. Witt,⁴⁹ J. Wood,⁷ J. Wu,³⁷ N. Xu,²¹ Q.H. Xu,²¹ Z. Xu,³ P. Yepes,³⁵ I-K. Yoo,³³ V.I. Yurevich,¹¹ W. Zhan,²⁰ H. Zhang,³ W.M. Zhang,¹⁹ Y. Zhang,³⁷

Z.P. Zhang,³⁷ Y. Zhao,³⁷ C. Zhong,³⁸ R. Zoukarnееv,¹² Y. Zoukarnееva,¹² A.N. Zubarev,¹¹ and J.X. Zuo³⁸

(STAR Collaboration)

- ¹Argonne National Laboratory, Argonne, Illinois 60439
²University of Birmingham, Birmingham, United Kingdom
³Brookhaven National Laboratory, Upton, New York 11973
⁴California Institute of Technology, Pasadena, California 91125
⁵University of California, Berkeley, California 94720
⁶University of California, Davis, California 95616
⁷University of California, Los Angeles, California 90095
⁸Carnegie Mellon University, Pittsburgh, Pennsylvania 15213
⁹Creighton University, Omaha, Nebraska 68178
¹⁰Nuclear Physics Institute AS CR, 250 68 Řež/Prague, Czech Republic
¹¹Laboratory for High Energy (JINR), Dubna, Russia
¹²Particle Physics Laboratory (JINR), Dubna, Russia
¹³University of Frankfurt, Frankfurt, Germany
¹⁴Institute of Physics, Bhubaneswar 751005, India
¹⁵Indian Institute of Technology, Mumbai, India
¹⁶Indiana University, Bloomington, Indiana 47408
¹⁷Institut de Recherches Subatomiques, Strasbourg, France
¹⁸University of Jammu, Jammu 180001, India
¹⁹Kent State University, Kent, Ohio 44242
²⁰Institute of Modern Physics, Lanzhou, China
²¹Lawrence Berkeley National Laboratory, Berkeley, California 94720
²²Massachusetts Institute of Technology, Cambridge, MA 02139-4307
²³Max-Planck-Institut für Physik, Munich, Germany
²⁴Michigan State University, East Lansing, Michigan 48824
²⁵Moscow Engineering Physics Institute, Moscow Russia
²⁶City College of New York, New York City, New York 10031
²⁷NIKHEF and Utrecht University, Amsterdam, The Netherlands
²⁸Ohio State University, Columbus, Ohio 43210
²⁹Panjab University, Chandigarh 160014, India
³⁰Pennsylvania State University, University Park, Pennsylvania 16802
³¹Institute of High Energy Physics, Protvino, Russia
³²Purdue University, West Lafayette, Indiana 47907
³³Pusan National University, Pusan, Republic of Korea
³⁴University of Rajasthan, Jaipur 302004, India
³⁵Rice University, Houston, Texas 77251
³⁶Universidade de Sao Paulo, Sao Paulo, Brazil
³⁷University of Science & Technology of China, Hefei 230026, China
³⁸Shanghai Institute of Applied Physics, Shanghai 201800, China
³⁹SUBATECH, Nantes, France
⁴⁰Texas A&M University, College Station, Texas 77843
⁴¹University of Texas, Austin, Texas 78712
⁴²Tsinghua University, Beijing 100084, China
⁴³Valparaiso University, Valparaiso, Indiana 46383
⁴⁴Variable Energy Cyclotron Centre, Kolkata 700064, India
⁴⁵Warsaw University of Technology, Warsaw, Poland
⁴⁶University of Washington, Seattle, Washington 98195
⁴⁷Wayne State University, Detroit, Michigan 48201
⁴⁸Institute of Particle Physics, CCNU (HZNU), Wuhan 430079, China
⁴⁹Yale University, New Haven, Connecticut 06520
⁵⁰University of Zagreb, Zagreb, HR-10002, Croatia

(Dated: October 29, 2018)

We report measurements of transverse momentum p_t spectra for ten event multiplicity classes of p-p collisions at $\sqrt{s} = 200$ GeV. By analyzing the multiplicity dependence we find that the spectrum shape can be decomposed into a part with amplitude proportional to multiplicity and described by a Lévy distribution on transverse mass m_t , and a part with amplitude proportional to multiplicity squared and described by a gaussian distribution on transverse rapidity y_t . The functional forms of the two parts are nearly independent of event multiplicity. The two parts can be identified with the soft and hard components of a two-component model of p-p collisions. This analysis then provides the first isolation of the hard component of the p_t spectrum as a distribution of simple form on y_t .

I. INTRODUCTION

The structure of the inclusive p_t spectrum from relativistic nuclear collisions is affected by several aspects of collision dynamics and by the final-state hadronization process. Comparisons of p-p, d-Au and Au-Au p_t spectra at RHIC suggest that a form of color-deconfined matter has been created in Au-Au collisions [1, 2]. Particle production mechanisms which could determine spectrum structure include soft parton scattering followed by longitudinal or ‘string’ fragmentation [3] and hard parton scattering followed by transverse fragmentation [4]. Other mechanisms could be significant. The structure of the p_t spectrum at some achievable level of precision may therefore be complex. A summary of efforts to unfold and interpret the structure of inclusive p_t spectra from ISR to Fermilab and SPPS energies in the context of jet phenomenology and QCD (quantum chromodynamic) theory is provided in [5].

At RHIC energies hard parton scattering is expected to dominate the spectrum at larger p_t and to be significantly modified in A-A collisions (jet quenching) [4, 6]. But how does hard scattering contribute at smaller p_t ? How does it interact with thermal or ‘soft’ particle production? Is there an ‘intermediate’ p_t region [7] with its own unique production mechanisms? Those issues remain unresolved after much theoretical speculation and experimental measurement and provide a context for the present analysis applied to high-statistics p_t spectra from ten multiplicity classes of p-p collisions. The multiplicity dependence offers new access to underlying particle production mechanisms.

p_t spectra from relativistic nuclear collisions are conventionally modeled by the *power-law* function [8], a form suggested by measured jet systematics and perturbative QCD (pQCD) expectations. At larger p_t the spectrum is expected to tend asymptotically to the power-law form p_t^{-n} [9]. The strict power-law form is then generalized to the function $A/(1 + p_t/p_0)^n$, having the expected pQCD dependence at larger p_t but transitioning to an approximate Maxwell-Boltzmann form at smaller p_t , consistent with expectations for thermal particle production. Although the power-law function has been previously applied to p-p data with apparently good fit quality (χ^2 within expected limits) it has not been tested with the precision of recently-acquired RHIC p-p data. One can question the validity of its underlying assumptions. For instance, why should a single model function adequately describe spectra which may represent a mixture of several particle production mechanisms?

Alternatively, a model function can be formulated in terms of the *two-component* model of nuclear collisions [10], which identifies ‘soft’ p-p collisions with no hard parton scatter and ‘semi-hard’ collisions with at least one significant parton scatter (*i.e.*, producing

distinguishable hadron fragments). According to the two-component model the minimum-bias distribution on event multiplicity n_{ch} can be decomposed into separate negative binomial distributions (NBD) identified with soft and semi-hard event types. We then expect the *fraction* of events with a hard parton collision to increase monotonically with selected event multiplicity n_{ch} . Variation of p_t spectra with n_{ch} could then provide a basis for isolating soft and hard (and possibly other) components of inclusive spectra on a statistical basis, where the hard spectrum component refers to the fragment p_t spectrum for hard-scattered partons, and the soft component is the p_t spectrum for ‘soft’ particle production.

In this analysis we first test the ability of the conventional power-law model function to represent the data. We then reconsider the data with no *a priori* assumptions. We attempt to describe all spectrum structure with the simplest algebraic model required by the data (*e.g.*, ‘simple’ in terms of parameter number and functional forms - *cf.* Eq. (4) and Sec. XI) and then to associate the model elements with possible particle production mechanisms. We adopt two new analysis techniques: 1) We introduce transverse rapidity y_t [11, 12] as an alternative to p_t . y_t has the advantage that spectrum structure associated with hard parton scattering and fragmentation is *more uniformly represented* on a logarithmic variable: y_t corresponds to variable $\xi_p = \ln(p_{\text{parton}}/p_{\text{fragment}})$ conventionally used to describe parton fragmentation functions in elementary collisions [13]. A simple description of soft particle production is not compromised by the choice of transverse rapidity. 2) We introduce the running integral of the y_t spectrum, which substantially reduces statistical fluctuations relative to significant structure and therefore improves the precision of the analysis.

In this paper we present high-statistics p_t spectra for ten multiplicity classes from p-p collisions at $\sqrt{s} = 200$ GeV. We use the conventional power-law model function to fit those spectra and assess the quality of that description. We then construct running integrals of the spectra on y_t and define a reference function common to all n_{ch} values and based on the Lévy distribution. We use that reference to extract difference spectra which contain the n_{ch} -dependent parts of the spectra in a more differential form. We find that the difference spectra have a simple structure: the major component is well-described by a gaussian distribution with fixed shape and with amplitude (relative to the reference) linearly proportional to the particle multiplicity. To simplify presentation we initially describe approximate relationships and optimized parameters without errors. We then return to a comprehensive discussion of the parameter system and its errors and consistency in Sec. VI. This analysis is based on p-p collisions at $\sqrt{s} = 200$ GeV observed with the STAR detector at the Relativistic Heavy Ion Collider (RHIC).

II. p_t AND y_t SPECTRA

Data for this analysis in the form of inclusive p_t spectra for unidentified charged particles were obtained from non-single-diffractive (NSD) p-p collisions at $\sqrt{s} = 200$ GeV triggered by a coincidence of two beam-beam counters (BBC) in $3.3 < |\eta| < 5$ [1]. Charged particles were measured with the STAR Time Projection Chamber (TPC) and Central Trigger Barrel (CTB) [14]. Particle momenta were determined with a 0.5 T magnetic field parallel to the beam (z) axis. Primary charged particles were represented by TPC tracks falling within the acceptance for this analysis – 2π azimuth, pseudorapidity $|\eta| < 0.5$, and $0.2 < p_t < 6$ GeV/c – and satisfying track cuts described in [1]. The *observed* particle multiplicity in the acceptance is denoted by \hat{n}_{ch} , whereas the corrected and p_t -extrapolated *true* event multiplicity is denoted by n_{ch} . From 3×10^6 NSD events individual p_t distributions were formed for 10 primary-particle multiplicity classes indexed by the observed multiplicity: $\hat{n}_{ch} \in [1, \dots, 8, 9 + 10, 11 + 12]$.

To eliminate backgrounds from event pileup each TPC primary-track candidate was independently required to match a CTB/trigger timing requirement (100 ns, matching efficiency 94%, false-coincidence background 2%) and project to the beam line within 1 cm transverse distance of closest approach. No other vertex requirement was applied to the primary tracks. The event-vertex z position was estimated by the arithmetic mean \bar{z} of projected track z for all CTB-matched primary tracks in an event. Events with $|\bar{z}| < 75$ cm were accepted for further analysis. The event vertex was not included in primary-track p_t fits. That procedure eliminated pileup-event tracks, selected those events well-positioned relative to the TPC and minimized correlations of individual track p_t and p_t spectrum shape with event multiplicity or event triggering not related to collision dynamics.

The resulting p_t spectra were corrected for tracking efficiency, backgrounds and momentum resolution. Tracking acceptance and efficiency on (p_t, η, z) and backgrounds were determined by embedding Hijing events in data events with at least one empty bunch (so-called abort-gap events). The same fractional correction was applied to all multiplicity classes. The correction factor was 1.45 at 0.2 GeV/c, falling to 1.2 at 0.5 GeV/c and thereafter smoothly to 1 at 6 GeV/c. Efficiency- and acceptance-corrected (but not p_t -extrapolated) spectra integrate to multiplicity $n'_{ch} = (1.35 \pm 0.015) \hat{n}_{ch}$, while the corrected *and* p_t -extrapolated per-event spectra integrate to ‘true’ multiplicity $n_{ch} = (2.0 \pm 0.02) \hat{n}_{ch}$. The errors reflect the spectrum-to-spectrum *relative* normalization uncertainties most relevant to this differential analysis. The normalization uncertainty common to all spectra is about 10%.

In Fig. 1 (left panel) corrected and normalized per-event p_t spectra are plotted as points in the form $1/n_{ch} 1/p_t dn/dp_t$ for ten multiplicity classes, offset by successive factors 40 (except for $\hat{n}_{ch} = 1$ at bottom).

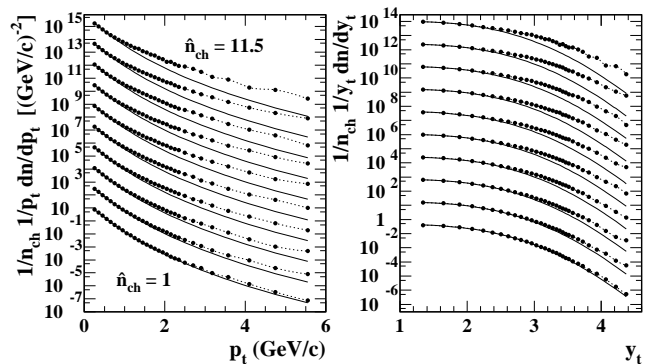


FIG. 1: Corrected and normalized charged-particle spectra on transverse momentum p_t (left) and transverse rapidity y_t (right) for 10 event multiplicity classes, displaced upward by successive factors 40 relative to $\hat{n}_{ch} = 1$ at bottom. Solid curves represent reference function $n_s/n_{ch} \cdot S_0(y_t)$ (cf. Sec. IV C). Dotted curves are spline fits to guide the eye.

Parentheses for ratio prefactors of spectrum densities in the form dn/dx are omitted to lighten notation. In other cases ratio prefactors are separated from densities by a dot. Corrected and extrapolated spectra normalized by n_{ch} all integrate to unity in the sense of Eq. (1) for p_t or y_t , with the integration limit $\rightarrow \infty$. In Fig. 1 (right panel) equivalent spectra on transverse rapidity are plotted. Hard parton scattering leading to transverse fragmentation may be better described on transverse rapidity $y_t = \ln\{(m_t + p_t)/m_0\}$, with transverse mass $m_t \equiv \sqrt{p_t^2 + m_0^2}$ and pion mass m_π assumed for m_0 : $y_t = 2 \Rightarrow p_t \sim 0.5$ GeV/c and $y_t = 4.5 \Rightarrow p_t \sim 6$ GeV/c. The solid curves $n_s/n_{ch} \cdot S_0$ provide a visual reference for the data. $n_s(\hat{n}_{ch})$ and $S_0(p_t$ or $y_t)$ are defined below, and function S_0 is by definition independent of \hat{n}_{ch} .

III. POWER-LAW ANALYSIS

The *power-law* function is the conventional model function applied to p_t spectra from relativistic nuclear collisions [8]. Said to be ‘QCD-inspired,’ the function $A/(1 + p_t/p_0)^n$ goes asymptotically to p_t^{-n} at large p_t (hence ‘power-law’) and approximates an exponential at small p_t . The argument supporting the power-law function assumes that p_t spectra at larger collision energies can be modeled with a single functional form. In this part of the analysis we test that assumption. The p_t spectra for ten multiplicity classes in Fig. 1 were fitted with the three-parameter power-law model function defined above. Parameters A , p_0 and n were independently varied to minimize χ^2 for each multiplicity class (in all fitting χ^2 was calculated using only statistical errors). The inclusive mean p_t was extracted for each class as $\langle p_t \rangle \equiv 2p_0/(n - 3)$ (cf. Sec. VII for those results).

In Fig. 2 (left panel) we plot *relative* fit residuals $\sqrt{y_t N_{evt}} (\text{data} - \text{fit}) / \sqrt{\text{data}}$ distributed on y_t . The

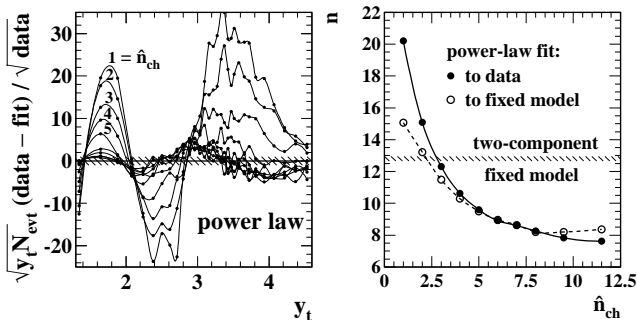


FIG. 2: Left: Relative residuals from power-law fits to p_t spectra in Fig. 1. The hatched band represents the expected statistical errors for STAR data. Right: Exponents n from power-law fits to data (solid points) and to corresponding two-component fixed-model functions (open circles, see Sec. VI) compared to the two-component fixed-model Lévy exponent 12.8 ± 0.15 (hatched band).

points indicate the actual data positions. The quantity plotted insures that the residuals are directly measured in units of the *r.m.s.* statistical error at each y_t . These relative residuals are then similar to Pearson’s correlation coefficient or relative covariance [15]. Poisson errors apply to dn/dy_t , whereas the spectra plotted in Fig. 1 (‘data’) are of the form $1/y_t dn/dy_t$. Thus, a factor $\sqrt{y_t}$ is required to make the statistical reference uniform on y_t in these residuals plots. The residuals structure on p_t is equivalent to that on y_t within a Jacobian factor (the fits were actually done on p_t and the residuals transformed to y_t for this plot). As noted in the discussion of Fig. 10 and elsewhere, much of the structure due to hard scattering and fragmentation is displaced to small p_t in a nonlinear way when plotted on p_t .

The large-wavelength residuals in Fig. 2 (left panel) exceed the expected statistical error (hatched band) by up to $30\times$ and are similar in form for various \hat{n}_{ch} classes, revealing a large systematic disagreement between the power-law model and data. The small-wavelength structure, mainly attributable to true statistical fluctuations, is consistent with expectations (hatched band). The argument supporting the power-law model of p_t spectra is thus shown to fail when tested with high-statistics STAR p-p data.

In Fig. 2 (right panel) we plot best-fit values of power-law exponent n vs \hat{n}_{ch} resulting from fits to data (solid points) and to the two-component model functions described later in this paper (open circles). The latter points and hatched band are discussed in Sec. XI. We observe a very strong variation of n with multiplicity. Reduction of n with increasing hard scattering is expected in the power-law context, but we find that the physical mechanism is different from the theoretical expectation (*cf.* Sec. XI).

We observe very strong disagreement between the power-law model function and data, whereas a previous UA1 (SPPS) analysis reported power-law fits with rea-

sonable χ^2 at the same energy [8]. The UA1 results are nevertheless consistent with the present analysis because that analysis was inclusive on n_{ch} and employed only 20k minimum-bias events (*vs* 3×10^6 for the present analysis). That analysis was therefore statistically insensitive to the structures apparent in Fig. 2. Statistics for the UA1 minimum-bias p_t spectrum are comparable to the $\hat{n}_{ch} = 11.5$ multiplicity class in this study, but the latter contains about $10\times$ the hard component in the UA1 minimum-bias spectrum. An E735 (FNAL) analysis of spectrometer data at 0.3, 0.55, 1.0 and 1.8 TeV [16], including multiplicity dependence of spectrum shapes, also obtained satisfactory power-law fits to p_t spectra. However the effective event number was comparable to the UA1 study, in part because of the reduced angular acceptance of the spectrometer relative to the STAR CTB detector, and the p_t acceptance [0.15,3] GeV/c was considerably less than STAR or UA1, further reducing sensitivity to spectrum shape. Given this exclusion of the power-law model we now seek an alternative model which best describes p_t spectra from relativistic nuclear collisions.

IV. RUNNING INTEGRATION

Running integration provides substantial noise reduction for spectrum analysis, thereby improving precision. In this section we examine the n_{ch} dependence of differential and integrated spectra and define alternative normalization factor $n_s(\hat{n}_{ch})$ and reference function S_0 .

A. Spectrum normalization

In Fig. 3 (left panel) the spectra from Fig. 1 (right panel) are replotted without vertical offsets as spline curves for detailed comparison. No assumptions have been made about the data, and all spectra integrate to unity when extrapolated. The dash-dot curve is reference S_0 defined in this section. To facilitate the discussion we identify three regions on y_t separated by the vertical dotted lines: A = [1.3,1.9], B = [1.9,3.4] and C = [3.4,4.5]. The region below $y_t = 1.3$ is outside the p_t acceptance. Regions A and C are defined such that the curves within them are nearly constant relative to one another, whereas in region B the differences between curves vary rapidly.

The trend of the spectra with increasing \hat{n}_{ch} is counterbalancing changes within A and C: linear decrease in A (see inset) and linear increase in C. The relative variation in the two regions over the observed \hat{n}_{ch} range is quite different: 10% reduction in A and $10\times$ increase in C. Such balancing variations are expected if the yield in C increases relative to A with \hat{n}_{ch} , due to the requirement that the normalized spectra must integrate to unity. We conclude that with increasing \hat{n}_{ch} additional particle yield localized on y_t and dominating region C is added to the spectrum.

The apparent reduction at smaller y_t is then a trivial effect of the unit-integral condition which can be compensated by changing the normalization. We normalize the spectra not by true total multiplicity n_{ch} but by multiplicity n_s defined such that the normalized spectra approximately coincide within region A. The variation of lower end-point positions with \hat{n}_{ch} is compensated within errors by normalizing with the linear function $\tilde{n}_s(\hat{n}_{ch}) = 2\hat{n}_{ch}(1 - 0.013\hat{n}_{ch})$ (function \tilde{n}_s estimates multiplicity n_s). The negative term compensates the relative yield increase at larger y_t . The revised normalization also facilitates the running integration study described below.

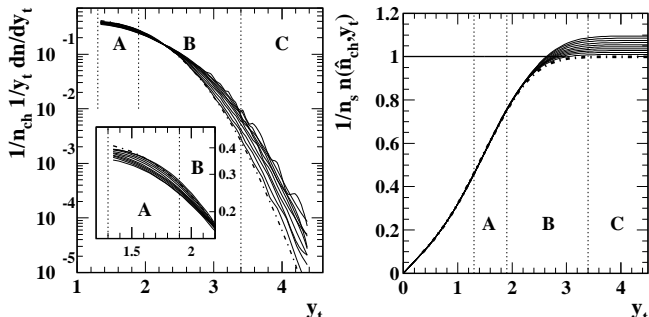


FIG. 3: Left: Spectra from Fig. 1 (right panel) replotted as spline curves and without offsets (solid curves) compared to reference S_0 (dash-dot curve). Right: Running integrals Eq. (1) of extrapolated y_t spectra in Fig. 1 divided by n_s/n_{ch} (solid curves) compared to running integral $N_0(y_t)$ of reference $S_0(y_t)$ (dash-dot curve). The ten data curves from bottom to top correspond to increasing $\hat{n}_{ch} \in [1, 11.5]$.

B. Running integrals and reference S_0

To calculate running integrals the measured spectra are extrapolated in the p_t interval $[0, 0.2]$ GeV/c ($y_t \in [0, 1.15]$) with reference function $n_s/n_{ch} \cdot S_0$. The extrapolation is relatively insensitive to the S_0 parameters, insuring quick convergence of the S_0 optimization procedure described below. The running integral of a y_t spectrum is defined by

$$n(\hat{n}_{ch}, y_t) = \int_0^{y_t} dy'_t y'_t \{1/y'_t dn(\hat{n}_{ch}, y'_t)/dy'_t\}. \quad (1)$$

In Fig. 3 (right panel) the normalized running integrals $1/n_s(\hat{n}_{ch}) \cdot n(\hat{n}_{ch}, y_t)$ reveal the detailed structure of the spectra with much-improved signal-to-noise ratio. We observe that the integrals in the right panel indeed nearly coincide up to $y_t \sim 2$. Above that point (region B) the integrals separate. In region C the integrals all saturate, with nearly equal spacings between curves. That result provides a first detailed look at the localized (on y_t) additional yield which produces the n_{ch} dependence of the y_t spectrum shape.

Given the results in Fig. 3 (right panel) the natural choice for a reference is one which coincides with all data curves for $y_t < 2$ and defines a limiting case for the sequence of separated data curves at larger y_t . We therefore *define* the reference as the asymptotic limit of the y_t spectra (or their integrals) as $\hat{n}_{ch} \rightarrow 0$. For reasons discussed below we chose as a trial reference the Lévy distribution [17]

$$S_0(m_t; \beta_0, n) = A_s / (1 + \beta_0(m_t - m_0)/n)^n \quad (2)$$

defined on transverse mass m_t and suitably transformed to y_t . $\beta_0 \equiv 1/T_0$ is an inverse-slope parameter. We find that the Lévy distribution with optimized parameters (dash-dot reference curves in Fig. 3) coincides with the desired asymptotic form. Determination of parameters n and β_0 from the data is discussed in the next subsection. Amplitude $A_s(\beta_0, n)$ is defined by the unit-integral normalization requirement on S_0 .

The running integral of S_0 , the dash-dot curve in Fig. 3 (right panel) denoted by N_0 , is obtained by replacing the curly bracket in Eq. (1) with $S_0(y_t)$, in which case $n(\hat{n}_{ch}, y_t) \rightarrow N_0(y_t)$ (also, see the legend in Fig. 4 – right panel). N_0 is thereby defined as the limit as $\hat{n}_{ch} \rightarrow 0$ of the running integrals for the ten multiplicity classes. We can obtain a more differential picture by optimizing reference curve S_0 and subtracting it and its running integral N_0 from the data. Fig. 4 (left panel) discussed in the next subsection reveals the n_{ch} -dependent yield increase as a localized structure on y_t and is used to optimize S_0 . This differential procedure represents a new level of precision in spectrum analysis facilitated by the high-statistics STAR p-p data and the running-integral technique.

C. Optimizing reference S_0

In Fig. 4 (left panel) we plot the difference between running integrals $1/n_s(\hat{n}_{ch}) \cdot n(\hat{n}_{ch}, y_t)$ of the corrected spectra in Fig. 3 (right panel) and reference integral $N_0(y_t)$ (the dash-dot curve in that panel). In region B we observe a strong localized \hat{n}_{ch} dependence in the y_t spectra. The optimum parameters for S_0 are derived as follows. Inverse-slope parameter β_0 is adjusted to minimize residuals in region A of Fig. 4 (left panel). β_0 determines the *average slope* of the residuals in that region. Exponent n then determines the size of the *first step* in region C. n is adjusted so that the first step follows the nearly linear trend of n_{ch} dependence in that y_t interval. Amplitude $A_s(\beta, n)$ is determined by the unit-normalization requirement for S_0 .

Changing either β_0 or n in S_0 *does not alter* the step-wise variation with \hat{n}_{ch} of the data curves in the left panel above the first step. That structure is inherent in the data and unaffected by the reference choice (*cf.* Fig. 3 – right panel, before reference subtraction). The amplitude variation within region C is well represented by $n_h/n_s =$

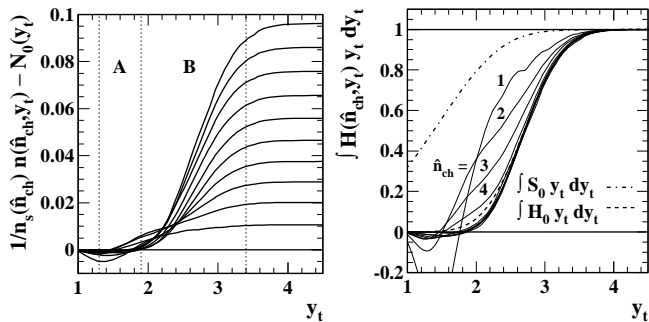


FIG. 4: Left: Differences between integrals of extrapolated y_t distributions in Fig. 1 according to Eq. (1), and integral $N_0(y_t)$ of soft reference $S_0(y_t)$. The ten curves correspond to $n_{ch} \in [1, 11.5]$ from bottom to top. Right: Distributions in the left panel divided by their end-point values at $y_t = 4.5$. The dashed curve is the running integral of H_0 (cf. Sec. V). The dash-dot curve is N_0 , the running integral of S_0 .

$\alpha \hat{n}_{ch}$ with $\alpha \sim 0.01$, where n_h is the coefficient of H_0 defined in the next subsection. That procedure determines reference S_0 parameters $A_s = 20.3 \pm 0.1$, $n = 12.8 \pm 0.15$ and $T_0 = 0.1445 \pm 0.001$ GeV [18].

In Fig. 4 (right panel) the curves are obtained by dividing the curves in the left panel by their values at upper endpoint $y_t = 4.5$ which approximate ratio n_h/n_s . Reference $N_0(y_t)$ is included in the right panel as the dash-dot curve. Comparing N_0 to the data integrals it is clear that the multiplicity dependence in Fig. 4 cannot be accommodated by adjusting S_0 . With the exception of the first few \hat{n}_{ch} values (labeled curves) the integrals closely follow a common trend: an error function or running integral of a gaussian which estimates *in a model-independent way* the running integral of the n_{ch} -independent model function $H_0(y_t)$ determined differentially in the next section.

V. DIFFERENTIAL ANALYSIS

Using running integrals we have defined a precision reference for the y_t spectra and isolated the n_{ch} dependence of those spectra relative to the reference. We now return to the differential y_t spectra and identify an additional spectrum component by subtracting the reference from the data. The dashed curve in Fig. 4 (right panel) (just visible near $y_t = 2$) represents the running integral of model function H_0 determined in this section. $H_0(y_t)$ models the additional yield at larger y_t as a differential y_t spectrum component. It is already clear from Fig. 4 that the shape of that component is approximately gaussian and nearly independent of n_{ch} .

In Fig. 5 (left panel) we show the result of subtracting reference $S_0(y_t)$ from the y_t spectra in Fig. 1 (right panel) divided by n_s/n_{ch} . We obtain the difference distributions denoted by $n_h/n_s \cdot H(\hat{n}_{ch}, y_t)$ (the data points connected with dashed curves). Those data represent *all* n_{ch} dependence of the y_t spectra relative to fixed reference S_0 .

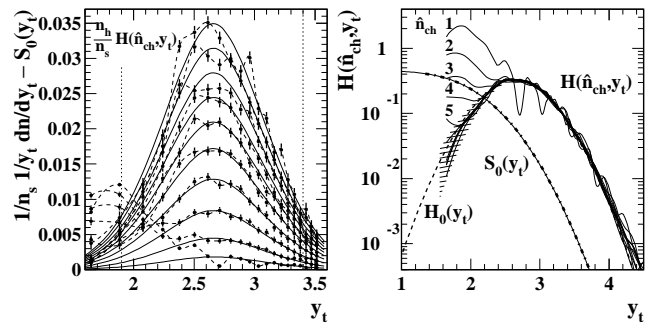


FIG. 5: Left panel: Distributions on y_t in Fig. 1 (right panel) divided by n_s/n_{ch} minus reference $S_0(y_t)$. Dashed curves in the left panel and solid curves in the right panel are spline fits to guide the eye. The vertical dotted lines enclose region B previously defined. Right panel: Distributions $H(n_{ch}, y_t)$ obtained by dividing the curves in the left panel by n_h/n_s . The dashed curve represents hard reference $H_0(y_t)$. The dash-dot curve represents soft reference $S_0(y_t)$. The solid curve underlying the dash-dot curve is an error function [19]. The hatched region estimates the systematic error from subtraction of S_0 .

The error bars denote statistical errors, applicable also to the data in Fig. 1. The two vertical dotted lines enclose region B on y_t previously defined. $H(\hat{n}_{ch}, y_t)$ has unit integral by definition, consistent with $n_s + n_h = n_{ch}$. The shapes of the data curves are well-approximated by the unit-integral gaussian reference

$$H_0(y_t; \bar{y}_t, \sigma_{y_t}) = A_h(\bar{y}_t, \sigma_{y_t}) \cdot \exp \left\{ -\frac{1}{2} \left[\frac{y_t - \bar{y}_t}{\sigma_{y_t}} \right]^2 \right\}, \quad (3)$$

with $A_h = 0.335 \pm 0.005$, $\bar{y}_t = 2.66 \pm 0.02$ and $\sigma_{y_t} = 0.445 \pm 0.005$. The solid curves represent $n_h/n_s \cdot H_0$, with best-fit amplitudes $n_h(\hat{n}_{ch})/n_s(\hat{n}_{ch})$ plotted in Fig. 7 (right panel, solid dots). n_h is the multiplicity of the new spectrum component. The data are generally well described by the model, except for the excursions at smaller y_t for the smaller \hat{n}_{ch} values.

Dividing the data in Fig. 5 (left panel) by the corresponding best-fit gaussian amplitudes n_h/n_s reveals the normalized data distributions $H(\hat{n}_{ch}, y_t)$ in the right panel. Reference $S_0(y_t)$, shown as the dash-dot curve in the right panel, is approximately an error function [19]. The hatched region estimates the systematic error from the S_0 subtraction. Deviations from the H_0 model function (dashed curve) in that panel represent *all* the residual n_{ch} dependence of the y_t spectra, *i.e.*, all deviations from the two-component model in Eq. (4) below. Those deviations are plotted in Fig. 6 (left panel) and discussed further in the next section.

The QCD-based power-law trend p_t^{-n} expected for hard parton scattering would appear in this plotting format as a straight line with negative slope equal to the exponent or ‘power’ $-n$ [5], since $y_t \sim \ln(2p_t/m_0)$ at large p_t makes the plot effectively a log-log plot. Out to $y_t = 4.5$ or $p_t = 6$ GeV/c we observe no linear tangential departure from gaussian model H_0 (dashed parabola) in

data $H(\hat{n}_{ch}, y_t)$.

VI. TWO-COMPONENT MODEL

The two-component model [10, 20] states that the minimum-bias frequency distribution on event multiplicity from relativistic p-p collisions can be resolved into two components, each approximated by a negative binomial distribution (NBD) with its own mean and k parameter. The two components correspond to events with (hard) and without (soft) significant hard parton scatters. That concept can be extended to the possibility that the inclusive p_t spectrum shape for hard events is different from that for soft events [21]—that the former contains an additional *spectrum* component which we designate the hard component, the complement being then the soft spectrum component. In that interpretation spectra from different multiplicity classes should contain different admixtures of the two spectrum components, and the multiplicity dependence of the spectrum shape may therefore provide a means to isolate those components.

In this section we examine the two-component model in detail. We consider the factorization structure of the model function that has emerged from data analysis, we examine the residuals structure compared to statistical errors and then test the *necessity* of the fixed-parameter model function by fitting the data with all model parameters freely varying. We finally relate all multiplicities in the model and show that they form a consistent system.

A. Two-component model function

We have analyzed the multiplicity dependence of y_t spectra from p-p collisions without an *a priori* model and have observed a strong n_{ch} dependence whose functional forms we now summarize. The two-component model of y_t spectrum structure can be generally represented by the first line of

$$\begin{aligned} 1/y_t \, dn/dy_t &= s(\hat{n}_{ch}, y_t) + h(\hat{n}_{ch}, y_t) \\ &= n_s(\hat{n}_{ch}) S_0(y_t) + n_h(\hat{n}_{ch}) H_0(y_t) + \dots, \end{aligned} \quad (4)$$

with unspecified soft and hard spectrum components $s(\hat{n}_{ch}, y_t)$ and $h(\hat{n}_{ch}, y_t)$. What we have inferred from the n_{ch} dependence of the measured y_t spectra is the second line, which represents a factorization hypothesis with spectrum components modeled by unit-normal functions $S_0(y_t)$ and $H_0(y_t)$ independent of n_{ch} , ratio $n_h(\hat{n}_{ch})/n_s(\hat{n}_{ch}) = \alpha \hat{n}_{ch}$, and constraint $n_s + n_h = n_{ch}$. We suggest that the algebraic model in the second line corresponds to the two-component physical model described above and represented by the first line. In the rest of this section we consider the quality and details of the parameterized model in Eq. (4) and test its uniqueness by performing a free χ^2 fit of the unconstrained model functions to the data.

In the power-law context there is no *a priori* hypothesis for n_{ch} dependence: each of the ten multiplicity classes in this analysis can be fitted independently with the three-parameter model to produce 30 fit parameters. The corresponding residuals are shown in Fig. 2 (left panel). For the two-component model we could in principle have six free parameters for each \hat{n}_{ch} , producing 60 fit parameters. However, the algebraic model of Eq. (4) (second line) contains constraints motivated by the requirement of model simplicity which greatly reduce the number of independent parameters. 1) The shapes of unit-integral functions $S_0(y_t)$ and $H_0(y_t)$ are independent of multiplicity: each function is determined by only two parameters fixed for all n_{ch} . 2) The relative normalization of the two components is nearly linearly proportional to the observed multiplicity, as defined by fifth parameter α . Thus, only five parameters represent all the data in that model. As with the power-law model we compare data to model on the basis of *relative* fit residuals on y_t , which provide a more differential and direct assessment of fit quality than the χ^2 statistic.

B. Five-parameter fixed model

The residuals in Fig. 6 (left panel) correspond to the function in the second line of Eq. (4) with five optimized parameters held fixed for all \hat{n}_{ch} . Above $y_t = 2.7$ the residuals are consistent with statistical fluctuations except for a few sharp structures with amplitude several times the statistical error. Those structures arise from the comparatively low statistics of the Monte Carlo simulations used for background corrections. The Monte Carlo statistical fluctuations appear in these residuals as small-wavelength systematic deviations.

The prominent residuals in $y_t < 2.7$ for $\hat{n}_{ch} = 1-4$ (a ‘third component’) could represent nontrivial n_{ch} dependence of the soft or hard component or some additional physical mechanism. The endpoint values at $y_t = 4.5$ in Fig. 4 (left panel) vary linearly with n_{ch} to a few percent (open symbols in Fig. 7 – right panel), despite the substantial nonlinear excursions at small y_t of the distributions in Figs. 5 and 6. That *apparent* contradiction suggests that the prominent residuals may represent a change of the hard component at small n_{ch} which preserves the linear trend of the integrals. These two-component residuals from the five-parameter fixed model are otherwise *much smaller* than the systematic deviations of the power-law model in Fig. 2 (left panel) with its 30-parameter χ^2 fit, especially in the large- y_t region where the power-law model should be most applicable.

C. Two-component free χ^2 fits

To determine whether the algebraic model of Eq. (4) is *necessary* (required by the data), not simply an accident of data manipulation, spectra for $\hat{n}_{ch} \in [1, 11.5]$ were fit-

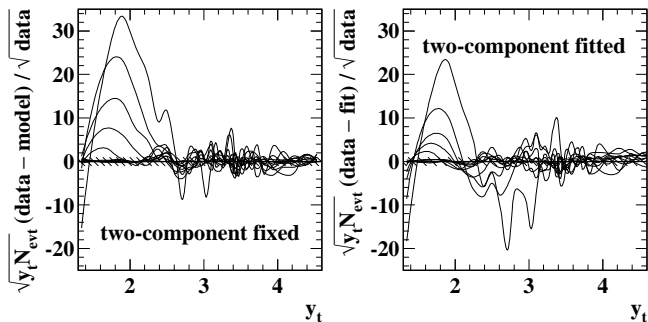


FIG. 6: Left: Relative residuals between data y_t spectra in Fig. 1 (right panel) and the two-component fixed parameterization, for all multiplicity classes. Right: Relative residuals between data y_t spectra and two-component free χ^2 fits, also for all multiplicity classes. The hatched bands represent the expected statistical errors for STAR data.

ted with the six-parameter function in Eq. (4) using χ^2 minimization. Spectra $1/y_t dn/dy_t$ were first normalized by multiplicity estimator $\tilde{n}_s(\hat{n}_{ch})$ from the fixed parameterization. The coefficients of S_0 and H_0 in the fitting function are then n_s/\tilde{n}_s and n_h/\tilde{n}_s . The six parameters ($n_s, \beta_0, n, n_h, \bar{y}_t, \sigma_{y_t}$) were freely varied for each \hat{n}_{ch} .

The residuals from the free fits are shown in Fig. 6 (right panel). The fit residuals are comparable to the corresponding fixed-model residuals in Fig. 6 (left panel), even though the free fits include six independent parameters for each of ten n_{ch} classes for a total of 60 parameters, compared to the fixed model with only five parameters to describe all ten n_{ch} classes. The residuals for the smaller \hat{n}_{ch} values show that the free fit attempts to minimize the small- y_t structure (‘third component’) in the left panel at the expense of increased intermediate- y_t residuals. The effect on the fit parameters is however modest, as illustrated in Table I.

Table I compares the fixed-model parameter values (fixed) to the results of the six-parameter free fits (fitted) for ten \hat{n}_{ch} classes. If the hard-component gaussian on y_t were not necessary we would expect the χ^2 fit to converge to the soft-component Lévy distribution as a proxy for the power-law function. The results in Table I indicate that most of the free-fit S_0 and H_0 shape parameters remain nearly constant within errors across the full \hat{n}_{ch} interval. The hard-component gaussian amplitudes are definitely nonzero and monotonically increasing, consistent with the trends in Fig. 5 (left panel) obtained by subtracting $S_0(y_t)$ from the normalized spectra in Fig. 1 (right panel).

Fig. 7 (left panel) shows trends for the two fit parameters n and n_h/\tilde{n}_s which best illustrate the trade-off between soft/power-law and hard components of the model and the necessity of the two-component model. Best-fit values are presented for all \hat{n}_{ch} classes as the solid symbols (open symbols are discussed below). There are significant systematic deviations of exponent n from the fixed-model value (hatched band) which are however

fitted	soft component			hard component			χ^2/ν
	\hat{n}_{ch}	n_s/\tilde{n}_s	$T_0(\text{GeV})$	n	n_h/\tilde{n}_s	\bar{y}_t	
1	0.995	0.145	11.97	0.000	—	—	73.3
2	1.001	0.145	11.78	0.002	2.75	0.500	40.4
3	1.001	0.145	11.83	0.013	2.75	0.421	15.0
4	0.996	0.145	11.74	0.025	2.75	0.400	7.36
5	0.994	0.145	12.60	0.049	2.65	0.427	3.14
6	1.001	0.144	15.63	0.089	2.57	0.450	1.09
7	0.999	0.144	15.42	0.097	2.57	0.451	0.62
8	1.005	0.144	16.73	0.115	2.56	0.454	1.18
9.5	1.011	0.143	16.66	0.130	2.56	0.456	0.52
11.5	0.995	0.145	15.69	0.128	2.58	0.460	1.20
fixed	1.000	0.1445	12.8	0.0105 \hat{n}_{ch}	2.66	0.445	
error	0.005	0.001	0.15	0.0005 \hat{n}_{ch}	0.02	0.005	

TABLE I: Two-component χ^2 fit parameters. The line labeled ‘fixed’ contains the two-component fixed-model parameters. Each fit has $\nu = 28$ degrees of freedom. The error row applies only to the fixed parameterization. The fit errors are generally smaller than those errors for the last five free-fit rows. Significant systematic effects are discussed in the text.

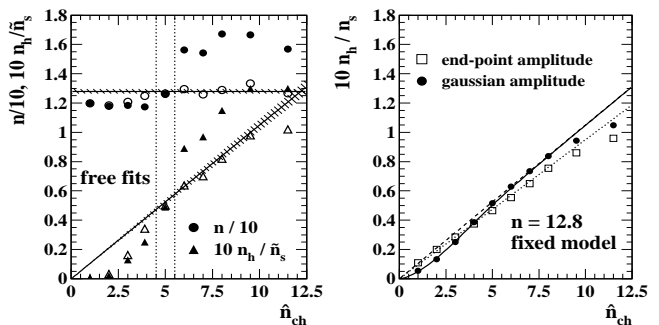


FIG. 7: Left: Parameters n and n_h/\tilde{n}_s vs \hat{n}_{ch} from free χ^2 fits (solid symbols) in Table I. The open symbols represent similar free fits but with \bar{y}_t held fixed at 2.65 (see text for discussion). The bands represent the corresponding two-component fixed parameterizations with their stated errors also given in Table I. Right: Ratio $n_h(\hat{n}_{ch})/n_s(\hat{n}_{ch})$ derived from integrals in Fig.4 (left panel) (open squares) and from gaussian amplitudes in Fig. 5 (left panel) (solid dots). The dashed and dotted lines have slopes 0.105 and 0.095 respectively. The solid curve is described in the text.

qualitatively different from the trends in Fig. 2 (right panel). The hard-component amplitude n_h/\tilde{n}_s also deviates from the linear fixed-model trend, but the trend of monotonic increase is even stronger. The hard component appears to be *more* favored by the free fit than by the fixed parameterization. We discuss the systematic differences between fixed model and free fit in the following paragraphs. However, this fitting exercise does demonstrate that for almost all \hat{n}_{ch} a two-component model is indeed necessary to describe RHIC p-p data.

The systematic deviations between free fits and fixed model in Fig. 7 (left panel) are easily understood. We

separately consider $\hat{n}_{ch} < 5$ and $\hat{n}_{ch} > 5$ (separated by the dotted lines). Generally, there is a strong positive correlation between soft-component exponent n and hard-component relative amplitude n_h/n_s originating from the requirement to describe the large- y_t yield. If n decreases the Lévy distribution tail rises and the amplitude of the hard-component gaussian amplitude must decrease as well to compensate at large y_t , and conversely. The systematic deviations relative to the fixed model for $\hat{n}_{ch} < 5$ respond to the presence of the ‘third component,’ which is not a part of the two-component model. To compensate for the additional component in the data the hard-component amplitude is suppressed and n is reduced by about 10% to provide additional yield from S_0 at small y_t . The consequence is negative residuals near $y_t = 2.6$ in Fig. 6 (right panel).

For $\hat{n}_{ch} > 5$ a different issue arises. In Fig. 5 (left panel) we have noted previously that the hard-component data peaks are skewed (fall off more rapidly on the low- y_t side) whereas the hard-component model function is a symmetric gaussian. The difference is most apparent in the running integrals of Fig. 4 (right panel): the dashed model curve lies above the data near $y_t \sim 2$. In Fig. 5 (right panel) the hatched region illustrates the region of maximum influence of the S_0 subtraction on the hard component. Because the hard-component data peaks are asymmetric the S_0 subtraction at larger y_t must be reduced by increasing exponent n (the small- y_t S_0 contribution must remain constant to describe the spectra there). This requires a compensating increase in the hard-component amplitude to fit the larger- y_t part of the spectra, and the gaussian model function must *shift down* on y_t (by ~ 0.1 or 5 sigma) and the width increase slightly (0.01 or 2 sigma) to accommodate the *apparent* increased symmetry of the data hard component.

To test that description the free fits were redone with the gaussian centroid fixed at $\bar{y}_t = 2.65$. The open symbols in Fig. 7 (left panel) show the result. The best-fit parameters are now within the error bands of the fixed model, with only modest increase in χ^2/ν (1.69, 1.07, 1.43, 0.95, 1.18 respectively for $\hat{n}_{ch} = 6, \dots, 11.5$ compared to the corresponding values in Table I). The fit residuals in Fig. 6 (right panel) appear identical for the two cases. We emphasize that the mode (most probable point) of the data hard-component peak is near $y_t = 2.65$. The downward shift of the *model* peak in the free fit is a consequence of the skewness in the data hard component not described by the fixed model but consistent with measured fragmentation functions from reconstructed jets.

D. Two-component multiplicities

In Sec. IV A we adopted a normalization strategy which brought all spectra into coincidence in region A of Fig. 3 (left panel) by defining multiplicity $n_s \propto \hat{n}_{ch}$ except for a small deviation linear in \hat{n}_{ch} . We then defined reference function S_0 as a limiting case of the spec-

trum n_{ch} dependence and isolated a second component H_0 by subtracting the fixed reference from all spectra. The amplitude of H_0 relative to the reference is defined by ratio $n_h/n_s \propto \hat{n}_{ch}$. The representation to that point is (physics) model independent, derived only from the observed spectrum \hat{n}_{ch} dependence: the reference is $\propto \hat{n}_{ch}$ and the second component is $\propto \hat{n}_{ch}^2$. That difference is the *underlying basis* for distinguishing the two components.

In this section we have identified the two algebraic spectrum components with the components of a physical model of soft and hard parton scattering and subsequent fragmentation to detected particles. We distinguish four event multiplicities: 1) the observed multiplicity \hat{n}_{ch} or uncorrected number of particles with $p_t > 0.2$ GeV/c in the STAR angular acceptance which serves as an event-class index, 2) the corrected and p_t -extrapolated multiplicity n_{ch} , 3) the ‘soft-component’ multiplicity n_s and 4) the ‘hard component’ multiplicity n_h , with $n_s + n_h = n_{ch}$. We now examine the self-consistency of the multiplicities in our two-component model in the context of real spectrum properties, including efficiencies and acceptances.

Soft multiplicity n_s is estimated by function $\tilde{n}_s(\hat{n}_{ch}) = [2.0 \pm 0.02(\text{rel}) \pm 0.2(\text{abs})] \hat{n}_{ch} [1 - (0.013 \pm 0.0005) \hat{n}_{ch}]$. The 1% error applies to the relative or spectrum-to-spectrum normalization relevant to this differential analysis, whereas the 10% error applies to the common normalization of all spectra. As noted, coefficient 0.013 is determined by requiring that corrected spectra normalized by \tilde{n}_s approximately coincide within region A of Fig. 3 (left panel) for all \hat{n}_{ch} . The factor 2 is determined by requiring that after correction, extrapolation with S_0 to $p_t = 0$ and normalization with n_{ch} all spectra in Fig. 1 integrate to unity. In the first column of Table I deviations of n_s/\tilde{n}_s from unity are consistent with the 1% error estimate.

The hard fraction $n_h/n_s = \alpha \hat{n}_{ch}$ is estimated by two methods. In the first method we determine the gaussian amplitudes required to fit the data distributions in Fig. 5 (left panel). Those amplitudes give the solid gaussian curves compared to data in that plot and are plotted as the solid points in Fig. 7 (right panel). The linear trend (dashed line) corresponds to slope $\alpha = 0.0105 \pm 0.0005$. The solid curve passing precisely through the points is $n_h(\hat{n}_{ch})/n_s(\hat{n}_{ch}) = \{(0.0105 \hat{n}_{ch})^{-10} + (0.005 \hat{n}_{ch}^{1.5})^{-10}\}^{-1/10}$, the errors on the coefficients being ± 0.0005 . The nonlinearity of that curve is related to the non-gaussian small- y_t structure for small values of \hat{n}_{ch} (third component).

In the second method we note that the distributions in the left panel of Fig. 4 are running integrals of data distributions in Fig. 5 (left panel). The amplitudes of those integrals at end-point $y_t = 4.5$, plotted as open squares in Fig. 7 (right panel), also estimate ratio n_h/n_s . They vary nearly linearly (dotted line) with slope $\alpha = 0.0095 \pm 0.0005$. Reduction of α from 0.0105 for the gaussian amplitudes to 0.0095 for the integral end-points results from small deviations of the data peaks

from the H_0 gaussian model at small y_t evident in Fig. 5. The data are slightly skewed in a manner consistent with measured fragmentation functions. The model gaussians are matched to the data at and above the data peak mode or most probable point. The integral of any data peak is therefore expected to be slightly less than that of the corresponding model function. Both methods suggest saturation of the hard-component amplitude at larger \hat{n}_{ch} .

Consistency of the soft and hard multiplicity estimators within the two-component model can be established by the following argument: Tracking inefficiencies produce the same fractional changes for all \hat{n}_{ch} and are represented by factors ϵ_s and ϵ_h for soft- and hard-component yields. The corrected spectra are extrapolated to $p_t = 0$ with soft model S_0 . The fraction of S_0 falling above $p_t = 0.2$ GeV/c (within the p_t acceptance) is represented by γ . The hard component identified in this analysis falls entirely within the p_t acceptance. The *observed* multiplicity is then given by $\hat{n}_{ch} \equiv \gamma\epsilon_s n_s + \epsilon_h n_h$, whereas the corrected and extrapolated spectra integrate to true multiplicity $n_{ch} = n_s + n_h$. The expression for \hat{n}_{ch} above can be rearranged to solve for n_s in the first line below,

$$n_s \simeq \frac{\hat{n}_{ch}}{\gamma\epsilon_s} \left\{ 1 - \frac{\epsilon_h}{\gamma\epsilon_s} \cdot \alpha \hat{n}_{ch} \right\} \quad \text{predicted} \quad (5)$$

$$\tilde{n}_s = 2\hat{n}_{ch} \{1 - 0.013 \hat{n}_{ch}\} \quad \text{observed}$$

whereas the second line is the estimator inferred from the data. By integrating reference S_0 we determine that $\gamma = 0.7$: 70% of the reference spectrum is within the acceptance $p_t > 0.2$ GeV/c. Tracking efficiencies ϵ_s and ϵ_h are both approximately 70%, and we have determined from the data (running integrals) that $\alpha \sim 0.0095$. We therefore have $1/\gamma\epsilon_s \sim 2$ and $\epsilon_h/\gamma\epsilon_s \cdot \alpha \sim 0.0135$, establishing the consistency (predicted \leftrightarrow observed) of the two-component multiplicities. Coefficient 0.013 is identified as α/γ , and the trend of n_s is defined by ratio $n_h/n_s = \alpha \hat{n}_{ch}$. We thus close the circle, demonstrating quantitatively how increase with \hat{n}_{ch} of the hard-component contribution to the spectrum forces n_s to decrease relative to \hat{n}_{ch} in compensation, why \tilde{n}_s contains the negative term and what its magnitude must be.

VII. $\langle p_t \rangle$ SYSTEMATICS

Another aspect of the two-component model is the variation of $\langle p_t \rangle$ (inclusive mean p_t) with \hat{n}_{ch} . Estimation of $\langle p_t \rangle$ for spectra with incomplete p_t acceptance requires either a model fit or direct integration of data with extrapolation. The power-law function for p_t distributions $1/p_t dn/dp_t = A/(1 + p_t/p_0)^n$, with $\langle p_t \rangle = 2p_0/(n - 3)$, has been used previously to extract $\langle p_t \rangle$ values from corrected p_t spectra [8]. $\langle p_t \rangle$ can also be determined by direct integration of the experimental p_t spectra, with extrapolation to $p_t = 0$ by a suitable model function. Finally, the two-component fixed-model function obtained in this analysis can provide a parameterization of $\langle p_t \rangle(n_{ch})$.

The running multiplicity integral $n(\hat{n}_{ch}, y_t)$ is defined by Eq. (1), with the data extrapolated over $p_t \in [0, 0.2]$ GeV/c by reference $n_s(n_{ch}) S_0(p_t)$. Running integral $p_t(\hat{n}_{ch}, y_t)$ can also be defined for transverse momentum p_t by including an extra factor $p_t(y_t)$ in the integrand of Eq. (1). The ratio $\langle p_t \rangle(\hat{n}_{ch}, y_t) = p_t(\hat{n}_{ch}, y_t)/n(\hat{n}_{ch}, y_t)$ is then a function of y_t for each value of \hat{n}_{ch} , and $\langle p_t \rangle(\hat{n}_{ch})$ is the limit of that function as $y_t \rightarrow \infty$. $\langle p_t \rangle(\hat{n}_{ch})$ is thus determined by direct integration of p_t or y_t spectra.

A changing mixture of soft and hard components may cause $\langle p_t \rangle$ to vary with n_{ch} . The $\langle p_t \rangle$ values for individual components are obtained by direct integration of model functions S_0 and H_0 : $\langle p_t \rangle_{soft} = 0.385 \pm 0.02$ GeV/c and $\langle p_t \rangle_{hard} = 1.18 \pm 0.01$ GeV/c. A two-component *analytic expression* for $\langle p_t \rangle$ is then given by

$$\langle p_t \rangle(\hat{n}_{ch}) = \left\{ 0.385 \frac{n_s(\hat{n}_{ch})}{n_{ch}} + 1.18 \frac{n_h(\hat{n}_{ch})}{n_{ch}} \right\} \text{ GeV/c,} \quad (6)$$

with $n_h/n_s = \alpha \hat{n}_{ch}$ and $n_s + n_h = n_{ch}$.

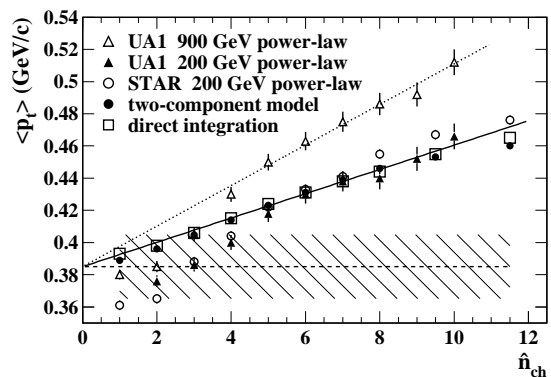


FIG. 8: $\langle p_t \rangle(\hat{n}_{ch})$ derived from the two-component H_0 gaussian amplitudes (solid dots), from the running integrals (open triangles) and from power-law fits to STAR and UA1 data (open circles, triangles). The solid and dotted lines correspond to Eq. (6) with $\alpha = 0.0095$ and 0.015 respectively.

In Fig. 8 $\langle p_t \rangle(\hat{n}_{ch})$ values inferred from power-law fits to corrected STAR spectra are represented by open circles, consistent with a 200 GeV UA1 power-law analysis plotted as solid triangles [8], but inconsistent at smaller \hat{n}_{ch} with the two-component result from this analysis plotted as solid points. The two-component data were obtained with the n_h/n_s values plotted as solid dots in Fig. 7 (right panel). The solid line represents the two-component analytic expression for $\langle p_t \rangle$ in Eq. (6) with $\alpha = 0.0095$. The UA1 results for 900 GeV [8] are plotted as open triangles. The dotted line corresponds to Eq. (6) with $\alpha = 0.015$. $\langle p_t \rangle$ values obtained by *direct integration* of the extrapolated spectra are represented by the open squares. The hatched region represents the common uncertainty in all means due to uncertainty in the particle yield in $p_t < 0.2$ GeV/c.

The $\langle p_t \rangle(\hat{n}_{ch})$ values in Fig. 8 obtained by direct integration of extrapolated spectra provide the best estimate of the physical trend. The results at 200 GeV for

direct integration, the two-component model and power-law fits are consistent within errors for $\hat{n}_{ch} > 4$. The notable deviation of the power-law results from the two-component linear trend for $\hat{n}_{ch} < 5$ can be explained by the third-component structures at small y_t and small \hat{n}_{ch} in Fig. 5 (left panel). Those structures strongly influence (bias) extrapolation of the power-law function into the unmeasured region in $p_t < 0.2$ GeV/c so as to overestimate the inferred yield there (nominally 30% of the total spectrum). The overestimate at small p_t produces a sharp reduction of $\langle p_t \rangle(\hat{n}_{ch})$ values inferred from power-law fits. The additional yield at small y_t in Fig. 5 itself corresponds to $\langle p_t \rangle \sim 0.4$ GeV/c, and thus cannot physically lower the composite $\langle p_t \rangle$ below $\langle p_t \rangle_{soft} = 0.385$ GeV/c. These $\langle p_t \rangle$ results demonstrate that the UA1 data are sensitive to the small- y_t and small- \hat{n}_{ch} structures revealed in this analysis when the more integral spectrum measure $\langle p_t \rangle$ is used.

VIII. ERRORS

The statistical errors for the basic y_t spectra in Fig. 1 are best indicated by the error bars on the difference distributions of Fig. 5 (left panel). That figure also compares the point-wise statistical errors to the hard-component structure inferred in this study, which is statistically well determined for all n_{ch} classes. Monte Carlo calculations of background corrections with full detector response simulation are computer intensive. Because of limited statistics the statistical fluctuations in the Monte Carlo data used for background corrections are injected into the corrected data spectra as visible systematic errors: long-wavelength systematic error is reduced at the expense of increased short-wavelength random ‘systematic’ error. Those errors are apparent as the nonstatistical short-wavelength structures in Figs. 2 and 6. The systematic uncertainties in the corrected spectra can be divided into n_{ch} -dependent and n_{ch} -independent uncertainties.

n_{ch} -independent systematic uncertainties include uncertainties in the corrections for tracking efficiency, backgrounds (mainly weak decays) and momentum resolution. Systematic spectrum corrections for this analysis were 20% or less, except for the lowest two p_t bins where they increased to 40%. Statistical errors for the systematic corrections were typically less than 1% (except as noted above for the background corrections). We estimate the uncertainties in the systematic corrections as 10% of the correction values. The total uncertainty for the systematic corrections is then less than 2% above $p_t = 0.4$ GeV/c. The UA1 corrected n_{ch} -inclusive p_t spectrum for 200 GeV \bar{p} -p collisions [8] agrees with the corresponding inclusive spectrum from the present analysis at the 2% level.

n_{ch} -dependent systematic errors could result from n_{ch} -dependent tracking inefficiencies. However, track detection and p_t measurement in this analysis required no

reference to other tracks or a fitted event vertex, thus minimizing any n_{ch} dependencies. In effect, each track was treated in isolation independent of its relationship to any event, except for the timing requirement with the CTB. The tracking efficiencies for low-multiplicity (1-4) and high-multiplicity (> 4) events integrated over the p_t acceptance were found to be consistent to 3%, with a 1% statistical error. We take that as an estimate of the n_{ch} -dependent systematic uncertainty.

The main source of systematic uncertainty in the shape of the hard-component structures isolated in Fig. 5 is the definition of S_0 as the lowest element of the regular sequence in Fig. 4 (left panel). S_0 is a rapidly-decreasing function in the interval $y_t = 1.6-3$. The main effect of varying either β_0 or n in S_0 is to change the magnitude of S_0 in that interval, shape changes being secondary. It is consistent within the two-component context to require that 1) component $H(n_{ch}, y_t)$ be non-negative, placing an upper bound on S_0 in Fig. 5 and 2) that any n_{ch} -independent aspect of the distributions in Fig. 5 be minimized, determining a lower bound. Those criteria place stringent constraints on S_0 already in $y_t \sim 1.6-2$, limiting systematic offsets at $y_t = 2$ to ± 0.002 , the allowed range rapidly decreasing above that point according to the S_0 curve in Fig. 10 (right panel). The systematic uncertainty estimate corresponding to those trends is represented by the hatched region in Fig. 5 (right panel).

The nonstatistical power-law fit residuals in Fig. 2 are as much as thirty times the statistical error. One of the findings of this study is that the power-law model function is inappropriate for these p_t spectra. Systematic uncertainties for the fit parameters are therefore not meaningful.

The fitting uncertainties for the fixed-model parameters are given at the bottom of Table I. Those uncertainties are meaningful relative to the fitting procedure defined in the two-component model context. The ability of that model to describe the data is apparent in Fig. 6 (left panel). The only significant residuals correspond to a low- y_t spectrum element (for $\hat{n}_{ch} = 1-4$) deliberately omitted from the two-component model. One source of systematic uncertainty in those parameters is whether the fixed-model prescription forces a certain result by excluding some other which may better describe the data.

To test that possibility a free χ^2 fit with all model parameters varying was conducted. The difference in the two cases is summarized in Table I and Fig. 7 (left panel). In particular, there are substantial differences in the Lévy exponent and the hard-component amplitude for the free fit depending on whether the position of the hard-component gaussian is constrained or not. When the gaussian position is constrained the free fit and the fixed model agree within the systematic uncertainties in the latter. The differences in the unconstrained fit are traced to significant departures of the shape of the hard component data peak from the symmetric gaussian peak shape: the model function could be further refined by adding a skewness (expected for fragmentation func-

tions) to improve the stability of the fits. However, it is not our purpose to develop a complex representation of y_t spectra, but rather to demonstrate the essential two-component aspects of the spectra with the simplest possible model function. The differences in fit parameters in Fig. 7 (left panel) can therefore be taken as a generous estimate of the systematic uncertainty in the fixed-component parameterization.

IX. IDENTIFIED PARTICLES

Model functions S_0 and H_0 derived from this analysis of unidentified particles represent physical spectrum components S and H for several hadron types, mainly π , K and p. Two questions emerge: 1) to what extent do S_0 and H_0 correspond to individual hadron types, and 2) to what extent does the n_{ch} dependence of the p_t spectrum truly separate two physical components S and H ? The soft component of one hadron species may have significant n_{ch} dependence which could be misinterpreted as the hard component of another species, or of the combination of unidentified hadrons in this study.

We can obtain some answers to those questions from n_{ch} -inclusive spectrum studies of identified hadrons. p_t spectra for $\sqrt{s_{NN}} = 200$ GeV p-p collisions have been measured for identified pions, kaons and protons [22]. Because $\hat{n}_{ch} \sim 1$ and the p_t acceptance was [0.3,3] GeV/c for that analysis the measured multiplicity-inclusive p_t spectra are reasonably described by Lévy distribution S_0 , especially the kaon and proton spectra. The common Lévy exponent for the three species is $n = 16.8 \pm 0.05$, compared to $n = 12.8 \pm 0.15$ measured in this analysis for unidentified hadrons. The slope parameter for identified pions is $T = 0.145 \pm 0.001$ GeV, whereas for both kaons and protons $T = 0.23 \pm 0.005$ GeV, compared to $T = 0.1445 \pm 0.001$ GeV for unidentified hadrons in this analysis.

The trend of S_0 with hadron species is easily understood. Addition of the ‘hotter’ K and p spectra to the ‘cooler’ pion spectrum flattens the unidentified hadron composite at larger p_t , reducing the exponent of S_0 to $n = 12.8$. At smaller p_t the pion fraction dominates the composite spectrum, and the unidentified-hadron slope parameter is the same as the pion slope parameter. The effect of the heavier hadrons on the composite spectrum is mainly to reduce the Lévy exponent from the larger physical value common to all three hadron species.

Information on the n_{ch} dependence of p_t spectra for identified particles is limited. A preliminary analysis of K_0^* and Λ p_t spectra up to 4 GeV/c [23] suggests that the n_{ch} dependence of both spectra can be described by a modest (5%) reduction of n with increasing n_{ch} . That trend can be compared to the free χ^2 fit results for S_0 in Table I as shown in Fig. 7 (left panel): n increases by about 25% over the measured \hat{n}_{ch} range. That increase is traced to an attempt by the model to accommodate a skewness of the hard component in the data, not a true variation in the soft component.

X. PYTHIA MONTE CARLO

A similar analysis of p-p collisions from the Pythia Monte Carlo [24] reveals substantial deviations from data. We studied default Pythia-V6.222 and Pythia ‘tune A’ (increased initial-state radiation and multiple soft parton scatters relative to the default) with parameters derived from studies of the underlying event in triggered jet events [25]. In Fig. 9 (left panels) we show Pythia p_t spectra normalized to unit integral and soft reference S_0 (dash-dot curves) determined by the same criteria applied to STAR data. Those plots can be compared to Fig. 3 (left panel). In Fig. 9 (right panels) we show the results of subtracting reference S_0 from the normalized spectra in the left panel divided by n_s/n_{ch} . Those plots can be compared to Fig. 5 (left panel). The dashed curves are the hard component H_0 for STAR data divided by 10 to provide a reference.

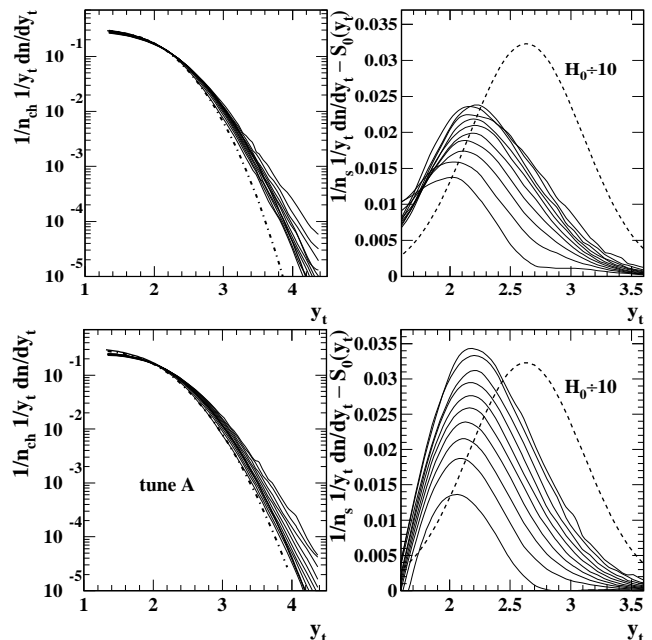


FIG. 9: Two-component analysis applied to Pythia Monte Carlo data with the same multiplicity classes as for STAR data. The left and right panels may be compared with Figs. 3 (left panel) and 5 (left panel) respectively. Dashed curves in the right panels represent the STAR data hard component for $\hat{n}_{ch} \sim 11$ ($H_0/10$). Dash-dot curves in the left panels represent soft component S_0 optimized for each Monte Carlo configuration: Pythia V6.222 default with parameters $T_0 = 0.147$ GeV and $n = 23$ (upper panel); Pythia Tune A with parameters $T_0 = 0.137$ GeV and $n = 14$ (lower panel).

The S_0 parameters for Pythia-V6.222 in the upper panels are $T_0 = 0.147$ GeV and $n = 23$. The large value of n implies that the Pythia soft component is nearly Maxwell-Boltzmann, in sharp contrast to RHIC data. The exponent is strictly limited to a large value by the Pythia data for $y_t < 2.5$. The S_0 parameters for Pythia tune A in the lower panels are $T_0 = 0.137$ GeV

and $n = 14$. The smaller value of n is comparable to the value 12.8 observed for RHIC data.

The hard-component yield for Pythia is generally a factor of two to three less than the data (most apparent above $y_t = 2.7$), broader and peaked at a smaller value of \bar{y}_t . Pythia-V6.222 shows a saturating of the hard-component amplitude with increasing \hat{n}_{ch} , whereas Tune A shows a more uniform and significantly greater rate of increase. The large gaussian-shaped offset *common to all curves* and centered at $y_t \sim 2$ is also not observed in the data. That structure cannot be accommodated by the Lévy distribution. The two Pythia Monte Carlos thus exhibit some features which agree qualitatively with experimental data but are quantitatively different. Tune A is closer to data than the default for soft and hard components, but the n_{ch} -independent gaussian offset near $y_t = 2$ persists and is not observed in the data.

XI. DISCUSSION

A description of p-p collisions in terms of soft and hard components is natural at RHIC energies where significant hard parton scattering occurs but the underlying event [25] is still relatively simple. The two-component model of nuclear collisions can be applied to 1) the event-frequency distribution on n_{ch} (two or more negative-binomial distributions) [10, 20], 2) the dependence of $\langle p_t \rangle$ on n_{ch} [8, 16, 26], 3) triggered jet correlations on (η, ϕ) (correlations from soft and hard event classes) [21] and 4) the n_{ch} dependence of the p_t or y_t spectrum shape [16]. The common theme is the relation of hard parton scattering to event multiplicity in the context of a ‘soft’ underlying event. This paper emphasizes analysis type 4) – study of the n_{ch} dependence of the spectrum shape on transverse momentum p_t and transverse rapidity y_t .

Model functions $S_0(y_t)$ and $H_0(y_t)$ in Eq. (4) can be viewed as the lowest-order elements of a perturbative expansion of the spectrum shape. Multiplicities $n_s(\hat{n}_{ch})$ and $n_h(\hat{n}_{ch})$ can be interpreted as estimating the mean numbers of soft- and hard-component particles per event for a given \hat{n}_{ch} . The claim of simplicity for the two-component fixed model is supported by the small number of parameters, the simplicity of the model functions, the demonstration of necessity in Sec. VIC and the demonstration with residuals plots that there is no additional information in the spectra (aside from the small- y_t ‘third component’ which may represent additional physics).

We cannot rule out additional components or changes in the shapes of *physical* components S and H . Each should be n_{ch} -dependent at some level, but the present analysis indicates that within the observed \hat{n}_{ch} interval any such dependence is near the level of statistical error. A change in S is suggested by the n dependence of the free χ^2 fits in Fig. 6 (left panel). However, that behavior may simply be due to a coupling of soft and hard amplitudes in the free fit, with no physical significance.

A significant change in H is expected at larger \hat{n}_{ch}

based on known jet physics: larger fragment multiplicities are produced by more energetic partons, with fragment distributions shifted to larger y_t [13]. Thus, the mean and width of H should increase with \hat{n}_{ch} at some point, but such changes are not observed beyond statistics within the y_t and \hat{n}_{ch} acceptances of this study. Apparently, the multiplicity increase in this analysis is dominated by increased *frequency of events with a single hard scattering* within a multiplicity class rather than bias toward more energetic partons. That scenario is consistent with the two-component model of [10].

The soft-component Lévy distribution $S_0 \equiv A_s/(1 + \beta_0(m_t - m_0)/n)^n$ [17] is similar in form to power-law function $A/(1 + p_t/p_0)^n$. However, the physical interpretations are quite different. The Lévy distribution describes a nominally exponential function with a control parameter (*e.g.*, slope parameter) which undergoes gaussian-random fluctuations. Inverse exponent $1/n$ then measures the *relative variance* σ_β^2/β_0^2 of the control parameter [27]. In the limit $1/n \rightarrow 0$ the Lévy distribution on m_t becomes a true Maxwell-Boltzmann distribution. Those properties suggested the Lévy distribution as a reference function for this analysis. Ironically, the ‘power-law’ function in the form of a Lévy distribution describes the soft component, not hard parton scattering. The Lévy parameters can be interpreted in the context of an ensemble of hadron emitters with random transverse speeds, thermal radiation from moving sources as described by the Cooper-Frye formalism [28]. The expected QCD hard-scattering power-law trend is not evident in the data out to $p_t \sim 6$ GeV/c.

In Fig. 2 (right panel) we plot exponent n values from power-law fits to data (solid points) and to the two-component fixed model (open circles) for the full range of \hat{n}_{ch} . The latter procedure simulates a power-law fit to data with no small- y_t excursions or ‘third component’ and illustrates the effect of those features on the exponent. The range of variation of the power-law exponent, in contrast to the two-component fixed model, and the substantial effect of the ‘third component’ further illustrate that the power-law parameterization is sensitive to aspects of spectra inconsistent with its theoretical motivation, making fit results difficult to interpret physically.

The gaussian shape of $H_0(y_t)$ inferred from this analysis can be compared with *fragmentation functions* from jet analysis of p-p, e-p and e-e collisions plotted on logarithmic variable $\xi_p \equiv \ln\{p_{jet}/p_{fragment}\}$, which also have an approximately gaussian shape [29] explained in a QCD context as the interplay of parton splitting or branching at larger p_t and the nonperturbative cutoff of the branching process at smaller p_t due to gluon coherence [30, 31]. The gaussian parameters are predicted by the pQCD MLLA (modified leading-log approximation) [32]. The hard component obtained in this analysis then represents not fragmentation functions from reconstructed large- E_t jets but rather the average of a *minimum-bias* ensemble of fragmentation functions dominated by *low- Q^2* parton scatters ($Q < 10$ GeV). In that context H_0 represents

minimum-bias partons dominated by *minijets* [33]. A previous study of small- E_t clusters in 200 GeV p-p collisions [34] suggested that semi-hard parton scattering or gluon radiation from projectile constituent quarks could produce substantial small- p_t structure in hadron spectra similar to the hard component of this study.

A recent analysis of p_t spectra in the interval 0.3 – 10 GeV/c for identified particles in p-p and d-Au collisions [35] used the relativistic-rise particle identification scheme to extend the spectra with very good statistics to large p_t . That paper compared the spectra to several NLO pQCD calculations and compared the m_t spectra of pions and protons. It concluded that there is a transition region from soft to hard particle-production processes at $p_t \sim 2$ GeV/c in inclusive particle production, which would appear to contradict the present results. However, the identified-particle spectra in that study below $p_t = 2.5$ GeV/c are from a previous study [22] in which the point-to-point systematic errors and the statistical errors are quite large, the latter due to the small acceptance of the prototype ToF detector. The ToF-based studies of multiplicity-averaged p-p collisions are therefore not sensitive to the hard-component structure reported in this paper, the great majority of which falls below 2.5 GeV/c. The present study takes a new approach by comparing large-statistics inclusive-hadron spectra in several multiplicity bins. Since the hard component is relatively enhanced in high-multiplicity events we are able to extend our investigation of the hard component to low p_t by studying the trend of that enhancement.

The relative frequency of hard scatters in p-p collisions is described by the fifth model parameter $\alpha \sim 0.01$, representing the nearly-linear dependence of n_h/n_s on \hat{n}_{ch} . We relate the hard-component amplitude to the frequency of hard collisions ($f \equiv$ number of hard collisions per NSD p-p collision) as $n_h(\hat{n}_{ch}) = \alpha \hat{n}_{ch} n_s(\hat{n}_{ch}) = f(\hat{n}_{ch}) \cdot \bar{n}_{mj}$, with mean true event multiplicity $\bar{n}_{ch} = 2.5$ in one unit of pseudorapidity and mean minijet multiplicity $\bar{n}_{mj} = 2.5 \pm 1$ [36]. We then estimate the observed frequency of hard scatters in $\sqrt{s} = 200$ GeV p-p collisions as $f = \bar{n}_h/\bar{n}_{mj} = 0.012 \pm 0.004$ observed hard scatters per NSD p-p collision per unit of pseudorapidity. In that interpretation multiplicity \hat{n}_{ch} serves as a ‘trigger’ for hard parton scattering, determining the fraction of hard-scattering events in a given multiplicity class and thus the relative amplitude of the hard spectrum component.

Model functions S_0 and H_0 on p_t and y_t are summarized in Fig. 10, which can be compared with Figs. 1, 3 and 5. $H_0/9 \Rightarrow n_h/n_s = 0.11$ is compared to data for $\hat{n}_{ch} = 11.5$ and illustrates the role of the hard component in the measured spectra with sufficient amplitude to be visible in a linear plotting format (right panel). Similarly, $H_0/140 \Rightarrow n_h/n_s = 0.007$ is compared to data for $\hat{n}_{ch} = 1$. Those coefficients are consistent with the measured hard-component gaussian amplitudes for $\hat{n}_{ch} = 1$ and 11.5 (*cf.* Fig. 7 – right panel).

Collisions in the event ensemble containing at least one semi-hard parton scatter within the detector acceptance

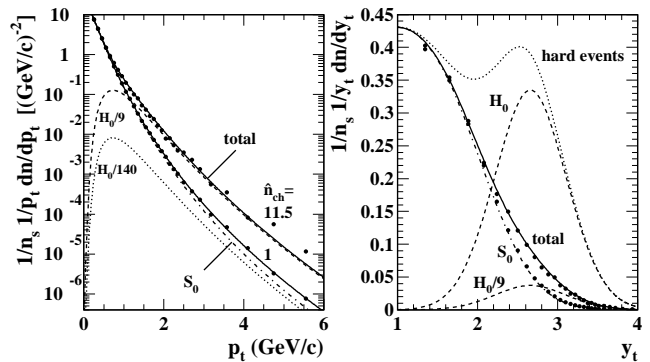


FIG. 10: Decomposition of inclusive p_t spectra into a soft component represented by a Lévy distribution on m_t and a hard component represented by a gaussian on y_t . Dashed curves $H_0/9$ correspond to data for $\hat{n}_{ch} = 11.5$, while dotted curve $H_0/140$ correspond to data for $\hat{n}_{ch} = 1$ (*cf.* Fig. 1). The dash-dot curves are soft reference S_0 , and the solid curves are the totals of soft and hard components for the model. The dotted curve in the right panel estimates the shape of the inclusive y_t distribution for those p-p collisions containing at least one minimum-bias hard parton scatter (hard events).

should have similar yields of soft and hard components (assuming an average minijet multiplicity of 2.5). The average y_t spectrum for such hard events is illustrated by $S_0 + H_0$, shown as the dotted curve in Fig. 10 (right panel). We cannot isolate such hard events in an unbiased manner, but we can infer their structure by extrapolating the n_{ch} trends determined in this analysis.

The left panel of Fig. 10 indicates the loss of visual sensitivity to spectrum structure when spectra are plotted on p_t . The hard component can appear to be a continuation of the soft component, whereas in the right panel the two components are clearly separate functional forms. y_t provides a more balanced presentation of structure resulting from hard-scattered parton fragmentation, yet does not compromise study of the soft component, which is well-described by a simple error function on y_t [19]. The transverse and longitudinal fragmentation systems undergo similar physical processes and should therefore be compared in equivalent plotting frameworks. Just as y_z is preferred to p_z we prefer y_t to p_t .

XII. SUMMARY

In conclusion, we have studied the event multiplicity n_{ch} dependence of high-statistics transverse momentum p_t or transverse rapidity y_t spectra from p-p collisions at $\sqrt{s} = 200$ GeV. We have determined that the ‘power-law’ model function fails to describe the spectra for any n_{ch} , exhibiting large nonstatistical deviations from data. An earlier UA1 study reporting satisfactory power-law fits to data seems contradictory. However, it is statistically consistent with the present study because the UA1 data were derived from a much smaller event sample. We

have analyzed the shapes of the spectra with a running-integral technique and determined that the spectra can be described precisely by a simple five-parameter model function. The algebraic model can in turn be related to a two-component physical model of nuclear collisions.

The power-law function motivated by pQCD expectations for hard parton scattering better describes the soft component in the form of a Lévy distribution on m_t (two parameters). We observe for the first time that the hard component is well described by a gaussian distribution on transverse rapidity y_t , with shape approximately independent of multiplicity (two parameters). The hard-component multiplicity *fraction* increases almost linearly with event multiplicity (the fifth model parameter). A detailed comparison of (data – model) residuals from the two-component fixed model and from free fits with all two-component model parameters varied confirms that the two-component fixed model is required by the data.

The hard component may represent fragments from transversely scattered partons. The shape is consistent with fragmentation functions observed in LEP and PETRA e^+e^- and FNAL p- \bar{p} collisions. The stability of the hard-component shape with event multiplicity suggests that a gaussian distribution on y_t is a good representation of minimum-bias parton fragments. The relative abundance of soft and hard components at any y_t of course depends on y_t and n_{ch} , but most of the hard-component yield falls below 2.5 GeV/c. There is evidence for a small but significant third component at smaller y_t and smaller n_{ch} . Comparison with the Pythia Monte Carlo reveals qualitative differences from data.

We thank the RHIC Operations Group and RCF at BNL, and the NERSC Center at LBNL for their support. This work was supported in part by the Offices of NP and HEP within the U.S. DOE Office of Science; the U.S. NSF; the BMBF of Germany; IN2P3, RA, RPL, and EMN of France; EPSRC of the United Kingdom; FAPESP of Brazil; the Russian Ministry of Science and Technology; the Ministry of Education and the NNSFC

of China; IRP and GA of the Czech Republic, FOM of the Netherlands, DAE, DST, and CSIR of the Government of India; Swiss NSF; the Polish State Committee for Scientific Research; SRDA of Slovakia, and the Korea Sci. & Eng. Foundation.

APPENDIX A: SYMBOL DEFINITIONS

Below is a list of symbols and their definitions as used in this paper.

- y_t : transverse rapidity, replaces transverse momentum p_t to provide improved visual access to fragment distributions
- \hat{n}_{ch} : observed event multiplicity in the detector acceptance, also the event-class index
- n'_{ch} : efficiency- and acceptance-corrected multiplicity in the detector acceptance
- n_{ch} : corrected and p_t -extrapolated or ‘true’ multiplicity in the detector angular acceptance
- n_s : soft-component multiplicity in the acceptance
- \tilde{n}_s : particular function of \hat{n}_{ch} used to estimate n_s
- n_h : hard-component multiplicity in the acceptance:
 $n_s + n_h = n_{ch}$
- α : hard-component coefficient: $n_h/n_s \sim \alpha \hat{n}_{ch}$
- S_0 : unit-normal functional form of the soft component (Lévy distribution on m_t)
- N_0 : running integral of soft reference S_0
- H_0 : unit-normal functional form of the hard component (gaussian distribution on y_t)
- A, p_0, n : power-law model parameters
- A_s, β_0, n : soft-component Lévy distribution parameters, $1/\beta_0 = T_0$, the slope parameter
- $A_h, \bar{y}_t, \sigma_{y_t}$: hard-component gaussian parameters

-
- [1] J. Adams *et al.* (STAR Collaboration), Phys. Rev. Lett. **91**, 172302 (2003).
 - [2] S. S. Adler *et al.* (PHENIX Collaboration), Phys. Rev. Lett. **91**, 072301 (2003); B. B. Back *et al.* (PHOBOS Collaboration), Phys. Lett. B **578**, 297 (2004); I. Arsene *et al.* (BRAHMS Collaboration), Phys. Rev. Lett. **91**, 072305 (2003).
 - [3] B. Andersson, G. Gustafson, G. Ingelman and T. Sjöstrand, Phys. Rep. **97**, 31 (1983).
 - [4] X. N. Wang and M. Gyulassy, Phys. Rev. D **44**, 3501 (1991).
 - [5] M. J. Tannenbaum, Eur. Phys. J. C **43**, 329 (2005); J. Phys. Conf. Ser. **27**, 1 (2005).
 - [6] X. N. Wang, Eur. Phys. J. C **43**, 223 (2005)
 - [7] R. C. Hwa and C. B. Yang, Phys. Rev. C **67**, 034902 (2003); V. Greco, C. M. Ko and P. Lévai, Phys. Rev. Lett. **90**, 202302 (2003); R. J. Fries, B. Müller, C. Nonaka and S. A. Bass, Phys. Rev. Lett. **90**, 202303 (2003).
 - [8] C. Albajar *et al.* (UA1 Collaboration), Nucl. Phys. B **335**, 261 (1990).
 - [9] R. Blankenbecler, S. J. Brodsky, J. F. Gunion, Phys. Lett. B **42**, 461 (1972); R. F. Cahalan, K. A. Geer, J. Kogut, L. Susskind, Phys. Rev. D **11**, 1199 (1975).
 - [10] A. Giovannini and R. Ugoccioni, Phys. Rev. D **59**, 094020 (1999).
 - [11] Transverse rapidity $y_t = \ln\{(m_t + p_t)/m_0\}$ in a longitudinally co-moving frame ($p_z = 0$) is equivalent in form to longitudinal rapidity $y_z = \ln\{(E + p_z)/m_0\}$ in a transversely co-moving frame ($p_t = 0$).
 - [12] D. V. Minh and P. Carruthers, Phys. Rev. Lett. **31** (1973) 133.
 - [13] M. Z. Akrawy *et al.* (OPAL Collaboration) Phys. Lett. B, **247**, 617 (1990); D. Acosta *et al.* (CDF Collaboration), Phys. Rev. D **68**, 012003 (2003). O. Biebel, P. Nason

- and B. R. Webber, hep-ph/0109282.
- [14] K. H. Ackermann *et al.* (STAR Collaboration), Nucl. Instrum. Meth. A **499**, 624 (2003).
- [15] J. F. Kenney and E. S. Keeping, Mathematics of Statistics, Pt. 1, 3rd ed. Princeton, NJ: Van Nostrand, 1962.
- [16] T. Alexopoulos *et al.* (E735 Collaboration), Phys. Lett. B **435**, 453 (1998).
- [17] G. Wilk and Z. Włodarczyk, Physica **A305**, 227-233 (2002).
- [18] Soft-component $n = 12.8 \pm 0.15$ from this study compares with power-law $n = 11.8 \pm 0.4$ from p - \bar{p} collisions [8] where the power-law exponent represents soft *and* hard components: flatter p_t distributions require smaller n values.
- [19] The Lévy distribution on y_t is well approximated by an error function: $S_0(y_t; y_{t0}, \xi_{y_t}) = A(y_{t0}, \xi_{y_t}) \{1 + \text{erf}[-(y_t - y_{t0})/\xi_{y_t}]\}/2$. For these data $A = 0.454 \pm 0.005$, $y_{t0} = 2.03 \pm 0.02$ and $\xi_{y_t} = 0.76 \pm 0.03$.
- [20] S. G. Matinyan and W. D. Walker, Phys. Rev. D **59**, 034022 (1999).
- [21] D. Acosta *et al.* (CDF Collaboration), Phys. Rev. D **65**, 072005 (2002).
- [22] J. Adams *et al.* (STAR Collaboration), Phys. Lett. B **616**, 8 (2005).
- [23] M. Heinz (STAR Collaboration), J. Phys. G. **31**, S1011 (2005).
- [24] T. Sjöstrand, Comput. Phys. Commun. **82**, 74 (1994); T. Sjöstrand, L. Lönnblad, S. Mrenna and P. Skands, hep-ph/0308153.
- [25] T. Affolder *et al.* (CDF Collaboration), Phys. Rev. D **65**, 092002 (2002); D. Acosta *et al.* (CDF Collaboration), Phys. Rev. D **70**, 072002 (2004); R. Field and R. C. Group (CDF Collaboration), hep-ph/0510198.
- [26] D. Kharzeev and M. Nardi, Phys. Lett. B **507**, 121 (2001).
- [27] J. Adams *et al.* (STAR Collaboration), nucl-ex/0408012.
- [28] F. Cooper and G. Frye, Phys. Rev. D **10**, 186 (1974).
- [29] M. Z. Akrawy *et al.* (OPAL Collaboration), Phys. Lett. B **247**, 617 (1990).
- [30] C. P. Fong and B. R. Webber, Nucl. Phys. B **355**, 54 (1991).
- [31] Y. L. Dokshitzer, V. S. Fadin and V. A. Khoze, Phys. Lett. B **115** (1982) 242.
- [32] C. P. Fong and B. R. Webber, Phys. Lett. B **229**, 289 (1989); Y. L. Dokshitzer, V. A. Khoze, C. P. Fong and B. R. Webber, Phys. Lett. B **273**, 319 (1991).
- [33] K. Kajantie, P. V. Landshoff and J. Lindfors, Phys. Rev. Lett. **59**, 2527 (1987); A. H. Mueller, Nucl. Phys. B **572**, 227 (2000); G. C. Nayak, A. Dumitru, L. D. McLerran and W. Greiner, Nucl. Phys. A **687**, 457 (2001).
- [34] C. Albajar *et al.* (UA1 Collaboration), Nucl. Phys. B **309**, 405 (1988).
- [35] J. Adams *et al.* (STAR Collaboration), Phys. Lett. B **637**, 161 (2006).
- [36] $\bar{n}_{mj} \approx 2.5$ at $\sqrt{s} \approx 200$ GeV is estimated from jet multiplicity systematics in T. Affolder *et al.* (CDF Collaboration), Phys. Rev. Lett. **87**, 211804 (2001); see also the survey of fragment multiplicities from e^+e^- collisions in I. M. Dremin and J. W. Gary, "Hadron multiplicities," Phys. Rept. **349**, 301 (2001).